International Journal of Nanomedicine

Dovepress
open access to scientific and medical research

Open Access Full Text Article

ORIGINAL RESEARCH

The 3D-Printed Ordered Bredigite Scaffold Promotes Pro-Healing of Critical-Sized Bone Defects by Regulating Macrophage Polarization

Yaowei Xuan[1,*], Lin Li[2,*], Chenping Zhang[3,4], Min Zhang[1], Junkai Cao[1], Zhen Zhang[3,4]

[1]Department of Stomatology, The First Medical Centre, Chinese PLA General Hospital, Beijing, People's Republic of China; [2]State Key Laboratory of Military Stomatology & National Clinical Research Center for Oral Diseases & Shaanxi Clinical Research Center for Oral Diseases, Department of Periodontology, School of Stomatology, Fourth Military Medical University, Xi'an, People's Republic of China; [3]Department of Oral Maxillofacial-Head Neck Oncology, Shanghai Ninth People's Hospital, Shanghai Jiao Tong University School of Medicine, Shanghai, People's Republic of China; [4]College of Stomatology, Shanghai Jiao Tong University, National Center for Stomatology, National Clinical Research Center for Oral Diseases, Shanghai Key Laboratory of Stomatology, Shanghai, People's Republic of China

*These authors contributed equally to this work

Correspondence: Zhen Zhang; Junkai Cao, Tel/Fax +86 153-1779-7335; +86 139-0129-0992, Email zz_nirvana@163.com; caojk301@163.com

Background: Repairing critical-sized bone defects secondary to traumatic or tumorous damage is a complex conundrum in clinical practice; in this case, artificial scaffolds exhibited preferable outcomes. Bredigite (BRT, $Ca_7MgSi_4O_{16}$) bioceramic possesses excellent physicochemical properties and biological activity as a promising candidate for bone tissue engineering.

Methods: Structurally ordered BRT (BRT-O) scaffolds were fabricated by a three-dimensional (3D) printing technique, and the random BRT (BRT-R) scaffolds and clinically available β-tricalcium phosphate (β-TCP) scaffolds were compared as control groups. Their physicochemical properties were characterized, and RAW 264.7 cells, bone marrow mesenchymal stem cells (BMSCs), and rat cranial critical-sized bone defect models were utilized for evaluating macrophage polarization and bone regeneration.

Results: The BRT-O scaffolds exhibited regular morphology and homogeneous porosity. In addition, the BRT-O scaffolds released higher concentrations of ionic products based on coordinated biodegradability than the β-TCP scaffolds. In vitro, the BRT-O scaffolds facilitated RWA264.7 cells polarization to pro-healing M2 macrophage phenotype, whereas the BRT-R and β-TCP scaffolds stimulated more pro-inflammatory M1-type macrophages. A conditioned medium derived from macrophages seeding on the BRT-O scaffolds notably promoted the osteogenic lineage differentiation of BMSCs in vitro. The cell migration ability of BMSCs was significantly enhanced under the BRT-O-induced immune microenvironment. Moreover, in rat cranial critical-sized bone defect models, the BRT-O scaffolds group promoted new bone formation with a higher proportion of M2-type macrophage infiltration and expression of osteogenesis-related markers. Therefore, in vivo, BRT-O scaffolds play immunomodulatory roles in promoting critical-sized bone defects by enhancing the polarization of M2 macrophages.

Conclusion: 3D-printed BRT-O scaffolds can be a promising option for bone tissue engineering, at least partly through macrophage polarization and osteoimmunomodulation.

Keywords: bredigite, three-dimensional printing, osteoimmunomodulation, macrophage polarization, tissue engineering

Introduction

The limited regenerative potential of endogenous bone repair in critical-sized defects remains a substantial clinical challenge. Along with the advancement of tissue engineering technology, biomaterial scaffolds have gradually shown advantages over autologous bone grafts by overcoming their limitations as a new clinical strategy.[1–3] However, currently available scaffold biomaterials have deficiencies in complex bone regeneration applications, such as mismatched structural support, uncoordinated biodegradability and lack of osteoinductivity.[4,5] To overcome these shortcomings, recent cutting-edge biomaterials have been explored for bone tissue engineering.[6,7]

Received: 17 October 2022
Accepted: 29 January 2023
Published: 20 February 2023

Graphical Abstract

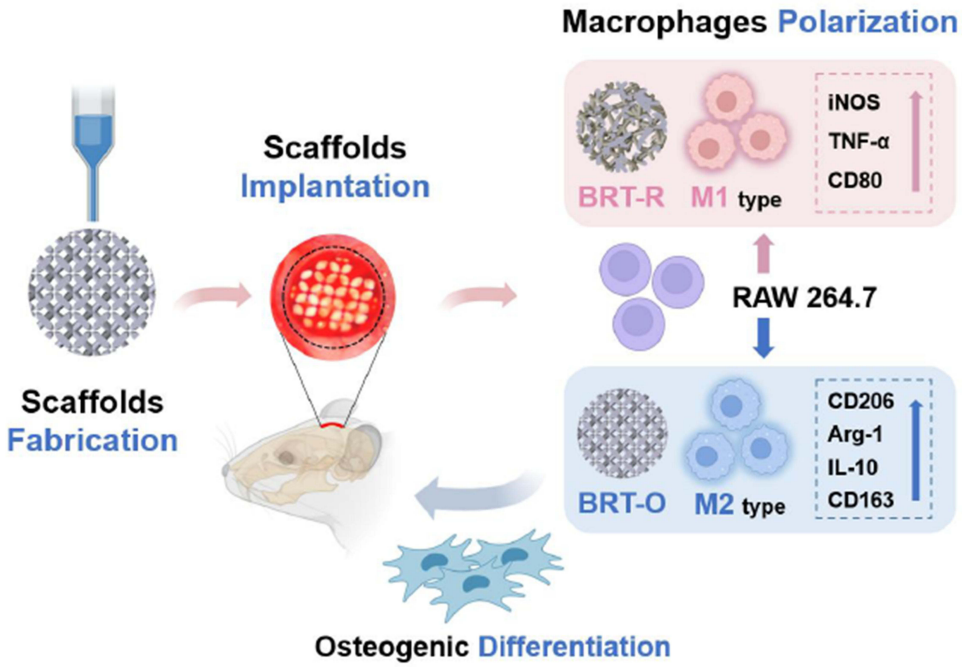

Considering their bioactive nature, magnesium-containing silicate bioceramics have been investigated as promising candidates for bone tissue engineering.[8] Bredigite (BRT, $Ca_7MgSi_4O_{16}$) contains various bioactive elements including calcium (Ca), magnesium (Mg), and silicon (Si).[9–11] Previous studies have demonstrated that BRT bioceramics possessed excellent biocompatibility, apatite-mineralization ability, and mechanical properties.[10–12] Furthermore, by releasing a variety of ionic products, BRT bioceramics may regulate the biological behavior of stem cells and enhance the ability of cell lineage differentiation.[13,14]

Based on the comprehension of osteoimmunology, the complex interaction between biomaterial and host cells is considered a determinant factor for the fate of biomaterial implantation.[15,16] Immediately after the implantation of bone biomaterial, the host immune response is initiated. As the key player in biomaterial-related immune reactions, macrophages were first activated as the pioneer, and significantly determined the long-term immune reactions. Moreover, macrophages promote the recruitment, proliferation, and differentiation of effector cells. Therefore, macrophages play vital roles in regulating immune response and osteogenesis in the bone defect area.[17–19] In addition, the dynamic nature and high plasticity of macrophages phenotype are essential features.[20] After receiving stimulation, macrophages are polarized into different functional states through different pathways, mainly M1 pro-inflammatory type and M2 anti-inflammatory type, which are involved in multiple physiological processes such as immunomodulation, tissue repair and regeneration, respectively.[21,22]

Studies indicate that characteristics of biomaterials, especially physicochemical properties, have important effects on macrophage polarization states.[21,23,24] The difference in the surface topology of biomaterials significantly shapes cell adhesion, morphology, and subsequent biological behavior and function, as well as determines the polarized fate of macrophages.[25–27]

Rapidly emerging three-dimensional (3D) printing technology is a digital manufacturing method that enables the quick preparation and precise manipulation of structural and morphological characteristics according to the requirements of targeted regenerative applications.[28] To facilitate bone defect repair and regeneration, porous scaffolds prepared by 3D printing technology with appropriately controlled biodegradability and good biocompatibility are usually employed as

matrix materials to support critical cells attachment and growth in the area of bone defects, and furthermore to induce the regeneration of the target tissues and recover organ functions.[29]

Previously, BRT scaffolds were fabricated by the 3D printing method, however the synthetic scaffolds were structurally inhomogeneous and randomly arranged.[1] In this study, we aimed to construct an ordered structural state of bredigite (BRT-O) scaffolds with better biological activity based on the excellent chemical properties for the first time using 3D printing method, and to further explore the role in modifying the immune microenvironment. The physico-chemical properties of BRT-O scaffolds and their effects on bone marrow mesenchymal stem cells (BMSCs) and macrophages were systematically investigated in vitro and in vivo.

Materials and Methods

Synthesis of the Bioceramic Scaffolds

The bredigite powder was synthesized by sol-gel process using tetraethoxysilane (TEOS, $Mg(NO_3)_2{\cdot}6H_2O$), magnesium dinitrate hexahydrate ($Mg(NO_3)^2{\cdot}6H_2O$), and calcium nitrate tetrahydrate ($Ca(NO_3)^2{\cdot}4H_2O$) and were ground in ethanol to get an average particle size ($\leq$ 80 μm). The bioinks for printing BRT scaffolds were prepared by thoroughly mixing sodium alginate (0.15 g) and BRT powders (5.0 g) in 3.0 g of Pluronic F-127 (20.0 wt %). The ink was then extruded through a nozzle with an inner diameter of 0.22 mm, controlled by Nano-Plotter software (GeSiM, Rossendorfer, Radeberg, Germany). The obtained primary BRT scaffolds were heated at a constant rate (2°C min^{-1}) and calcined for 3 hours at 1350°C. Following the Standard Tessellation Language file of 3D models, BRT scaffolds with ordered square hole structure (BRT-O) and scaffolds with random morphology (BRT-R) were prepared by laying patterns of filaments (0°/90°). In addition, β-tricalcium phosphate (β-TCP) scaffolds were also prepared as a control group. The dimensions of the prepared scaffolds were expanded to a designed size to compensate for the linear shrinkage in the three dimensions. The prepared scaffolds were sterilized by UV irradiation and used for subsequent biological experiments.

Physicochemical Characterization of the Scaffolds

The surface morphology of the fabricated scaffolds (BRT-O, BRT-R and β-TCP) was analyzed by scanning electron microscope (SEM, Inspect F, FEI, Eindhoven, Netherlands) while the phase composition was examined using an X-ray diffractometer (XRD, Rigaku Co., Tokyo, Japan) under 40 kV voltage and 40 mA current. Fourier transform infrared spectroscopy (FTIR, Thermo Nicolet Co., Waltham, MA, USA) was employed to analyze the chemical composition and spatial distribution. To test the compressive strength of the scaffolds, a universal mechanical testing machine (3367; Instron, Norwood, MA, USA) was utilized with a constant crosshead speed (0.5 mm/min). Five samples of each material were tested.

The scaffold degradations were evaluated regarding weight change, pH values and ionic release. For this purpose, the scaffolds (200 mg/mL) were soaked in 30 mL of Tris solutions (pH 7.4) at 37°C for six consecutive weeks, and the buffer solution was changed every 3 days. At the time-point of observation, the solutions of groups were collected and refreshed. Then, the scaffolds were removed and dried at 120°C for 24 h prior to accurate weight measurement. The changes in the pH value of the solutions were detected by a pH meter (Metrohm, Herisau, Switzerland). In addition, inductively coupled plasma atomic emission spectrometry (ICP-AES, Varian Inc., Palo Alto, CA, USA) was used to calculate the ionic concentrations of Ca, Si and Mg at different time periods.

Macrophages Biological Response to the Scaffolds

Murine macrophage cell line RAW 264.7 was purchased from the Typical Culture Preservation Commission Cell Bank, Chinese Academy of Sciences (Shanghai, China), and cultured in Dulbecco's Modified Eagle's Medium (DMEM, Sigma-Aldrich, St. Louis, MO, USA) containing 10% FBS (Gibco, Thermo Fisher Scientific, Inc., Waltham, MA, USA) and 100 U mL^{-1} penicillin /streptomycin (Hyclone, Logan, UT, USA). After culturing for 24 h, the morphology of RAW 264.7 cells seeding on different scaffolds was observed using SEM. Cell viability was performed by CCK-8 assay at 1, 3, and 5 days of culture. At the observation time-point, a 50 μL aliquot of CCK-8 solution (Sigma-Aldrich) was added to each well and incubated for 4 h. Then, the supernatants were extracted into a new well plate for absorbance measurement at

450 nm using a microplate reader (Rayto RT-6000, Rayto Co., Shenzhen, Guangdong, China). To assess the polarization phenotypes of macrophages seeded on different scaffolds for 24 h, flow cytometry was performed to detect the expression levels of the classical surface molecules such as CD80 and CD206. After collecting the cells, the corresponding antibodies (BioLegend Inc., San Diego, CA, USA) were incubated for 30 min and then detected by flow cytometry (Beckman Coulter Inc, Brea, CA, USA).

Immunofluorescence (IF) staining was performed to evaluate inducible nitric oxide synthase (iNOS, red, 1:200, ab49999, Abcam, Cambridge, UK) and CD 206 (red, 1:200, #24595, Cell Signaling Technology Corp., Danvers, MA, USA) expression levels after culturing for 24 h. Meanwhile, CD68 (green, 1:200, #29176, CST) as the pan marker, anti-F-actin antibody (red, 1:200, GTX20205, GeneTex, Irvine, CA, USA) for cytoskeletal protein staining and DAPI (blue, C1002, Beyotime Biotechnology, Shanghai, China) for nuclear staining were also used in this study. The macrophages were fixed in 4% paraformaldehyde and permeabilized with 0.25% Triton X-100 (Sigma-Aldrich), followed by blocking with 2% bovine serum albumin. After that, the primary and secondary antibodies were added. Laser scanning confocal microscopy (LSCM, Olympus Corp., Shinjuku, Japan) was utilized to visualize and capture images.

After RAW 264.7 cells were cultured on the scaffolds for 1 and 3 days, quantitative real-time PCR (qRT-PCR) was conducted to examine the transcriptional expression of iNOS, tumor necrosis factor-alpha (TNF-α), CD206 and arginase 1 (Arg-1), M1 and M2 macrophage polarization markers. The primers synthesized were as follows: mouse-GAPDH, GGCAAATTCAACGGCACAGTCAAG and TCGCTCCTGGAAGATGGTGATGG; mouse-iNOS, ATCTTGG AGCGAGTTGTGGATTGTC and TAGGTGAGGGCTTGGCTGAGTG; mouse-TNF-α, GGACTAGCCAGG AGGGAGAACAG and GCCAGTGAGTGAAAGGGACAGAAC; mouse-CD206, GTCTGAGTGTACGCAGT GGTTGG and TCTGATGATGGACTTCCTGGTAGCC; mouse-Arg-1, AACCTTGGCTTGCTTCGGAACTC and GTTCTGTCTGCTTTGCTGTGATGC. After 3 days of RAW 264.7 culture, the medium was centrifuged (2500 rpm) for 10 min to obtain the supernatants. Enzyme-linked immunosorbent assays (ELISA, Dakewe Bioengineering, Shenzhen, Guangdong, China) were performed to calculate the concentrations of cytokines, IL-10 and TNF-α in the supernatants according to the instructions.

The Biological Response of BMSCs to Polarized Macrophages

To investigate the effects of polarized macrophages on osteogenesis in vitro, BMSCs were isolated from the femurs and tibias of male C57BL/6N mice (aged 6–8 weeks, weighing 21–26 g) and cultured following the modified whole bone marrow adherent method. Briefly, the bone marrow tissues were cultured in complete culture medium composed of α-minimal essential medium (α-MEM; Gibco), 10% FBS (Gibco) and 100 U mL^{-1} penicillin/streptomycin (Hyclone) in a humidified incubator at 37°C with 5% CO_2. The adherent colonies were cultured for 7–10 days with medium changed every 3 days. The third to fifth passage cells (P3–5) were used for subsequent experiments. The obtained BMSCs were cultured with macrophages conditioned medium, which was derived from the supernatants of RAW 264.7 cells seeding on the β-TCP, BRT-R, and BRT-O scaffolds for 48 h culture. The vitality of BMSCs stimulated by the conditioned medium at 1 and 3 days was estimated by CCK-8 assay. In addition, the effect of macrophage polarization in response to different scaffolds on BMSCs migration was investigated by Transwell migration assay. Raw 264.7 cells were seeded on the scaffolds in the lower chambers, while BMSCs were plated in the upper chamber. After 24 h of incubation, the penetrated cells were stained and counted under an optical microscope (Olympus).

After osteogenic culture for 14 days, alkaline phosphatase (ALP) staining and ALP activity assays were performed following the instructions of the ALP assay kit (Sigma-Aldrich). Alizarin red S (ARS, Sigma-Aldrich) staining was conducted to evaluate calcium nodule formation on the 21st day of osteogenic culture, referring to the manufacturing instructions (Beyotime Biotechnology). The osteogenic induction medium was composed of a complete culture medium supplemented with 0.1 mM dexamethasone, 10 mM β-glycerophosphate, and 50 mM ascorbic acid (Sigma-Aldrich). The medium was changed every 3 days.

We administered qRT-PCR to evaluate the mRNA expression levels of osteogenic differentiation markers, bone morphogenetic protein-2 (BMP2) and runt-related transcription factor 2 (RUNX2) in BMSCs grown with macrophage conditioned medium after 3 days. The primers used are shown as follows: mouse-BMP2, ATCCAGTC TTGCCGCCTCCAG and CTTCGCCTCCTCCTCCTTCTCC; mouse- RUNX2, CCTTCAAGGTTGTAGCCCTC and

GGAGTAGTTCTCATCATTCCCG. To observe the morphology and cytoskeleton of BMSCs, F-actin (green, 1:200, GTX20205, GeneTex) and vinculin (red, 1:200, ab129002, Abcam) were stained by IF staining after culturing for 24 h as described above.

Bone Regeneration of the Scaffolds in the Rat Cranial Critical-Sized Defect Model

All animal procedures were approved by the Animal Experimental Ethics Committee at the Ninth People's Hospital affiliated with the Shanghai Jiao Tong University School of Medicine, China (Ref No: SH9H-2020-A610). The animal experiments were designed and executed in accordance with the Guidelines for Animal Health and Use of the National Institutes of Health, and reported following the ARRIVE guidelines. To explore the effects of different scaffolds on new bone formation in vivo, a total of 48 Sprague–Dawley rats (8–10 weeks, male) were randomly divided into 4 groups to construct critical-sized cranial defect models, including blank group, β-TCP group, BRT-R group, and BRT-O group. After general anesthesia, circular bone drills with a copious water coolant were used to fabricate 5-mm diameter defects on the parietal bone of rats bilaterally. Then, the prepared scaffolds (Φ5 mm×1 mm), including the β-TCP, BRT-R, and BRT-O scaffolds were implanted into the defects. In addition, the blank group without any scaffold materials was set as a control. Cefazolin (10 mg/kg) was given for 3 days to prevent infection, and the condition of the rats were observed daily. After 6 and 12 weeks postoperatively the rats were euthanized, the skull samples were collected to evaluate bone regeneration.

The samples (n=4 in each group) were fixed with 4% paraformaldehyde and examined under the micro-computed tomography system (μ-CT, Scanco Medical, Bassersdorf, Zurich, Switzerland) to evaluate the newly regenerated bone regions (70 kV voltage, 114 mA current, and 700-ms integration time). The ratio of bone volume to total tissue volume (BV/TV) was calculated using the μ-CT 80 system. The tissue blocks were sliced into 200 μm thickness of sections without decalcification using a hard tissue microtome (Leica, Wetzlar, Germany) and sequentially polished to a thickness of 25 μm. Toluidine blue staining solution was used for 15 min, and the sections were observed under an optical microscope (Leica).

Meanwhile, the collected tissues were decalcified with 15% EDTA and prepared into 10-μm-thick sections. Hematoxylin and eosin (H&E) staining was performed for the histological evaluation of the newly formed bone. The images were observed and captured by a stereoscopic microscope (Eclipse E600, Nikon, Tokyo, Japan). The proportion of new bone formation was calculated using Image-Pro Plus v.7.0 (Media Cybernetics Inc., Rockville, MD, USA). In addition, at one week postoperatively, the expression of the osteogenic marker, RUNX2 (1:100, GTX38531, GeneTex) was detected by immunohistochemical (IHC) staining (n=4 in each group).

Macrophage Polarization Adjustment of the Scaffolds in vivo

Regarding the scaffolds for osteoimmunomodulation in vivo, the expression of macrophage phenotype-related markers in the defects was examined by IHC staining. After one-week postoperatively, pan marker CD68 (1:200, ab125212, Abcam), M1 marker iNOS (1:200, ab15323, Abcam), and M2 marker CD163 (1:200, ab182422, Abcam) were labeled. The images of IHC staining were visualized under an optical microscope (Leica). Four non-overlapping fields of the view were picked randomly for each section under a microscope (20x).

Statistical Analysis

All quantitative data were expressed as mean ± standard deviation (x ± SD) and were analyzed using GraphPad Prism v.9.0 (La Jolla, CA, USA) software. One-way analysis of variance (ANOVA) and Tukey's multiple-comparisons test were utilized to perform data analysis. P values < 0.05 (two-sides) were accepted as statistically significant.

Results

Fabrication and Characterization of BRT-O

The prepared scaffolds were characterized for various structural parameters and mechanical properties. A clinically used β-TCP bioceramic was used as the control material. With a controlled design, the BRT-O scaffold demonstrated more

ordered gross morphology than the BRT-R scaffold. The SEM observation revealed the coarse surface of the β-TCP scaffold due to the scrambled deposition of β-TCP particles. High magnification SEM image showed clear grain boundaries and homogeneous pores size (400~500 μm) in case of the BRT-O scaffold (Figure 1A), which was favorable to facilitating the ingrowth of bone tissues.[5] The XRD analysis of three materials demonstrated that identical chemical structures along with bredigite peaks existed between the BRT-O and BRT-R scaffolds (Figure 1B). In addition, the FTIR spectra demonstrated the existence of PO_4^{3-} absorption bands from 900–1400 cm^{-1} in BRT ceramics (Figure 1C).

The compressive strength of the three scaffolds displayed significant differences (Figure 1D). The 3D-printed ordered BRT-O scaffold exhibited the highest compressive strength (>30 MPa) compared to the BRT-R scaffold, which ranged from 20~25 MPa and the β-TCP scaffold (~5 MPa). The weight changes of the scaffold materials soaked in Tris solution for six consecutive weeks were compared in Figure 1E. With the increase in soaking time, the materials presented a sustained degradation with 20% weight loss in BRT-O and BRT-R, which were higher than β-TCP (<5%). Figure 1F showed that the pH values of the Tris solution increased with the soaking time in the BRT-O and BRT-R groups, while the pH values of solution containing the β-TCP were reduced to 7.1 ± 0.02. Meanwhile, the BRT-O and BRT-R materials released higher concentrations of Ca, Si, and Mg ion comparing to the β-TCP scaffold and exhibited a similar ions release profile (Figure 1G).

The Effects of BRT-O on M2-Type Macrophage Polarization

To explore the effects of ordered interface on macrophage polarization, RAW 264.7 cells were seeded on the BRT-O, BRT-R, and β-TCP scaffolds. SEM images showed that the macrophages spread on the BRT-O scaffold surface along the

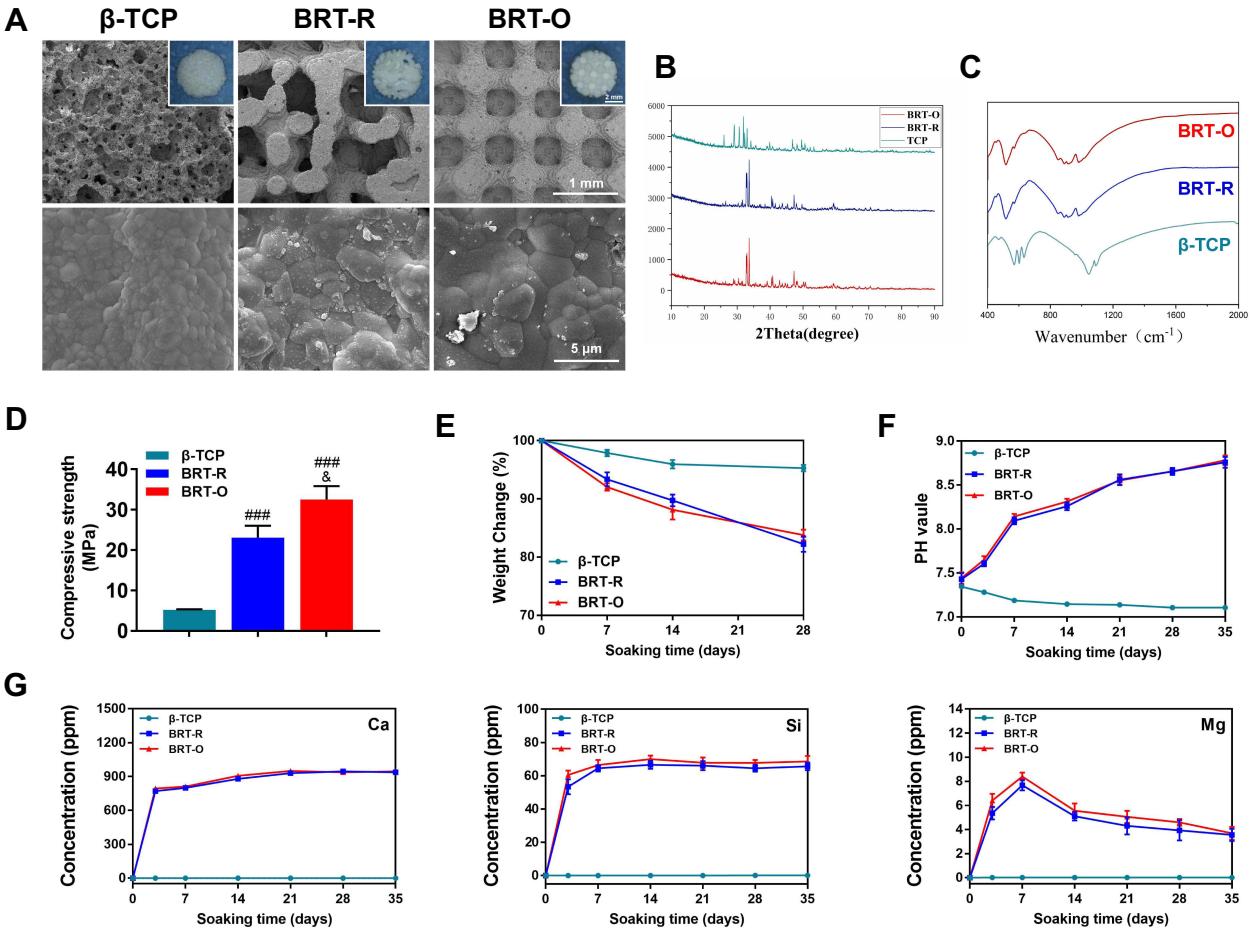

Figure 1 Characterization of the scaffolds. (**A**) Representative gross morphology (Scale bar, 2 mm) and surface topography SEM images (Scale bar, 1 mm and 5 μm). (**B**) X-ray diffraction patterns. (**C**) FTIR spectra. (**D**) Compressive strength. (**E**) Weight change of the scaffolds after soaking in Tris solution. (**F**) pH values. (**G**) Accumulated ionic release of Ca, Si, and Mg. Data are expressed as mean ± SD (n = 3). $^{\&}P < 0.05$ vs BRT-R scaffold; $^{\#\#\#}P < 0.001$ vs β-TCP scaffold.

cell fibrils (Figure 2A). CCK-8 assay demonstrated that macrophages cultured on different materials grew stably, and there were no significant differences in the absorbance values among groups (Figure 2B). CD80, iNOS, and TNF-α were used as M1 macrophage markers, while CD206, Arg-1, and IL-10 were considered the markers of M2 macrophage. After culturing for 24 h, flow cytometry analysis demonstrated that CD80 expression level was down-regulated in the BRT-O group, while CD206 expression was highly upregulated (Figure 2C). The IF staining revealed that the percentages of CD206+CD68+ M2 macrophages were higher in the BRT-O group relative to the other groups, whereas macrophages on the β-TCP surface highly expressed iNOS+CD68+ markers. Furthermore, macrophages grown on the BRT-O surface exhibited a highly branched, elongated morphology compared to the other groups (Figure 2D and E).

Transcriptional expression of macrophage polarization markers was assessed by qRT-PCR after culturing for 1 day and 3 days. The results showed that the mRNA expression levels of iNOS and TNF-α were markedly decreased in the BRT-O group, while the transcription of CD206 and Arg-1 were significantly increased. However, there was no significant difference in CD206 and Arg-1 expression between BRT-R and β-TCP groups (Figure 2F). In parallel, the TNF-α level was significantly reduced in the BRT-O scaffolds group, while the IL-10 level was increased as detected by ELISA (Figure 2G). Based on these findings, qRT-PCR examination, IF staining and flow cytometry results yielded a similar trend. Thus, the BRT-O scaffolds stimulated macrophage polarization to M2 phenotype.

Effects of Polarized Macrophages by BRT-O Scaffold on BMSCs Proliferation, Migration, and Differentiation in vitro

The biological behaviors of BMSCs cultured in macrophages conditioned medium exposed to different scaffold materials were detected. CCK-8 results revealed that BMSCs seeding on the scaffolds showed no significant difference in the absorbance (Figure 3A). Transwell migration assay of BMSCs in response to different materials and differentiated macrophages illustrated an enhanced penetration of BMSCs through Transwell membranes at the BRT-O group with a significant difference compared to the other groups (Figure 3B and C).

To further investigate the osteoinductive effects of differentiated macrophages induced by scaffolds in vitro, we detected BMSCs osteogenic differentiation qualitatively and quantitatively. According to the ALP detection and ARS staining data, the ALP activity and mineralization nodules formation of BMSCs were markedly enhanced in the BRT-O group, while no statistical difference was observed in the β-TCP group (Figure 3D–F). Moreover, mRNA expression levels of osteogenic differentiation-related genes (BMP2 and RUNX2) were significantly upregulated in the BRT-O group, followed by the BRT-R and β-TCP groups (Figure 3G), which was suggestive of a significant promotion of BMSCs osteogenic differentiation. IF staining observed that the cytoskeleton protein of BMSCs on the BRT-O group was highly extended with large attachment areas and high expression of adhesive plaque proteins (Figure 3H). Accordingly, M2-type macrophages polarized by the BRT-O scaffolds enhanced the migration and facilitated the osteogenic differentiation of BMSCs.

The Effects of BRT-O on Repairing Critical-Sized Bone Defects

After 6 and 12 weeks post-implantation, the cranial samples were collected for gross observation and μ-CT analysis to detect new-bone formation (Figure 4). According to the three-dimensional reconstruction images by μ-CT, the degradation of these scaffolds was increased with time from weeks 6 to 12. Accompanying with the biodegradation of the scaffold material at 12 weeks, the BRT-R group and BRT-O groups showed growth of well-integrated new bone formation into the scaffolds, while a sizeable residual void space was observed in the β-TCP group.

Toluidine blue staining was performed to observe the morphology and quantity of newly formed bone (Figure 5A). It is evident that the scaffold materials were further degraded over time, and the ingrowth of new bone tissue was significantly accelerated between weeks 6 and 12. Notably, in the BRT-O and BRT-R groups, new bone thrived along the material edges and peripheral region of the defects, which followed in situ bone island formation pattern. The defects in the BRT-O group were filled with the integrated new bone which was composed of mature structure based on the histological staining. No fibers or other pathological tissues existed between the scaffold material with the host bone, indicating excellent osseointegration between the scaffold material and the host bone. The quantity of newly formed bone

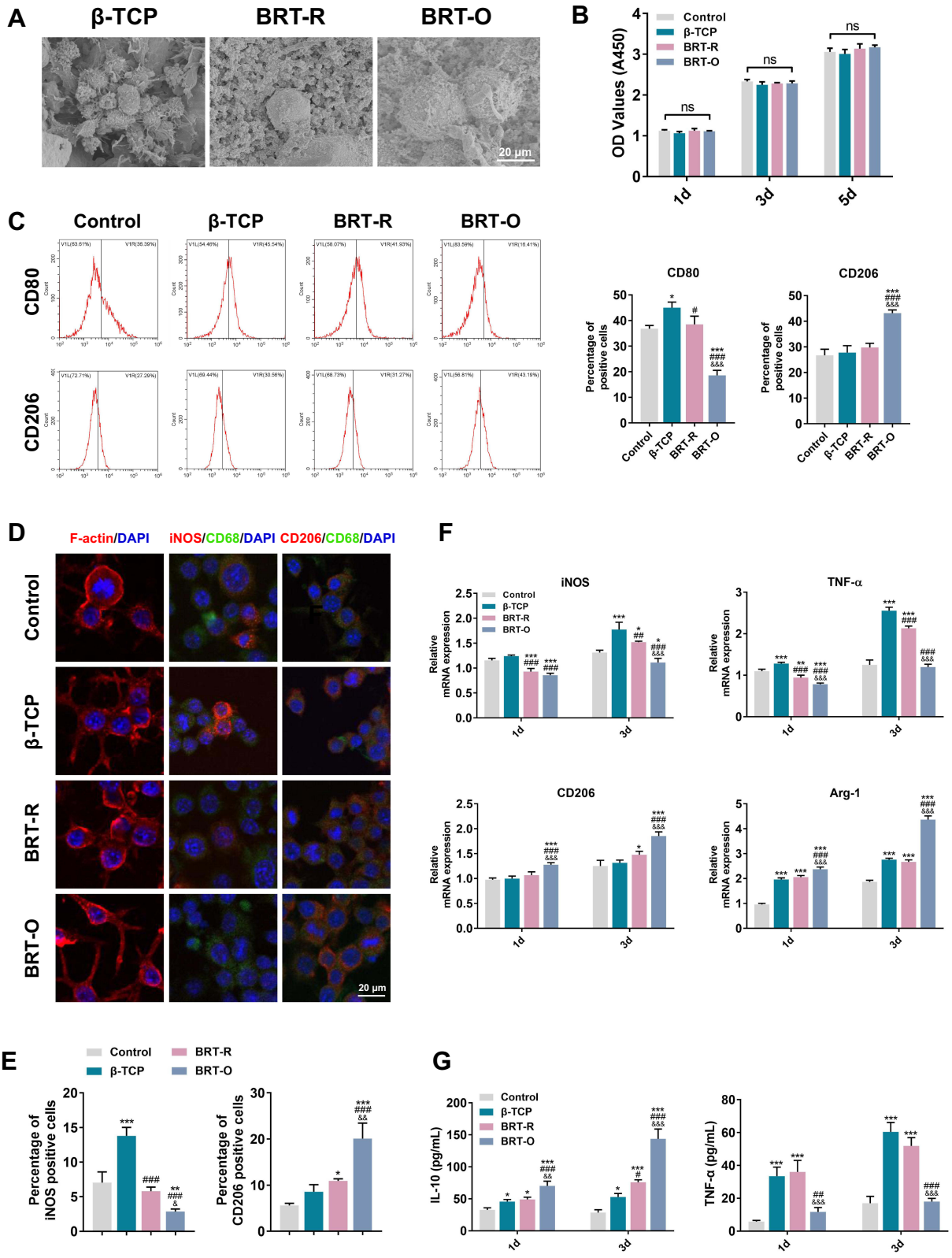

Figure 2 Biological behavior and polarization phenotype of macrophages cultured on the scaffolds. (**A**) Representative images of macrophage morphology as visualized by SEM. (**B**) CCK-8 assay results after 1, 3, and 5 days of cell culture. (**C**) Representative peak plots and quantification of CD80+ (M1 polarization) and CD206+ (M2 polarization) macrophage ratios examined by flow cytometry. (**D**) IF staining for phenotypic markers of macrophages was performed using F-actin (red), iNOS and CD206 (red), CD68 (green), and nuclei (blue) by LSCM. (**E**) Percentages of iNOS+ and CD206+ cells based on LSCM images. (**F**) mRNA expression levels of M1 polarization markers (iNOS, TNF-α) and M2 (CD206, Arg-1) in macrophages at 1 and 3 days as quantified by qRT-PCR. (**G**) IL-10 and TNF-α levels as detected by ELISA. Data are expressed as mean ± SD (n = 3). Scale bar, 20 μm. Ns, no significance; $^{*}P < 0.05$ vs Control group; $^{\#}P < 0.05$ vs β-TCP scaffold; $^{\&}P < 0.05$ vs BRT-R scaffold; $^{**}P < 0.01$ vs Control group; $^{\#\#}P < 0.01$ vs β-TCP scaffold; $^{\&\&}P < 0.01$ vs BRT-R scaffold; $^{***}P < 0.001$ vs Control group; $^{\#\#\#}P < 0.001$ vs β-TCP scaffold; $^{\&\&\&}P < 0.001$ vs BRT-R scaffold.

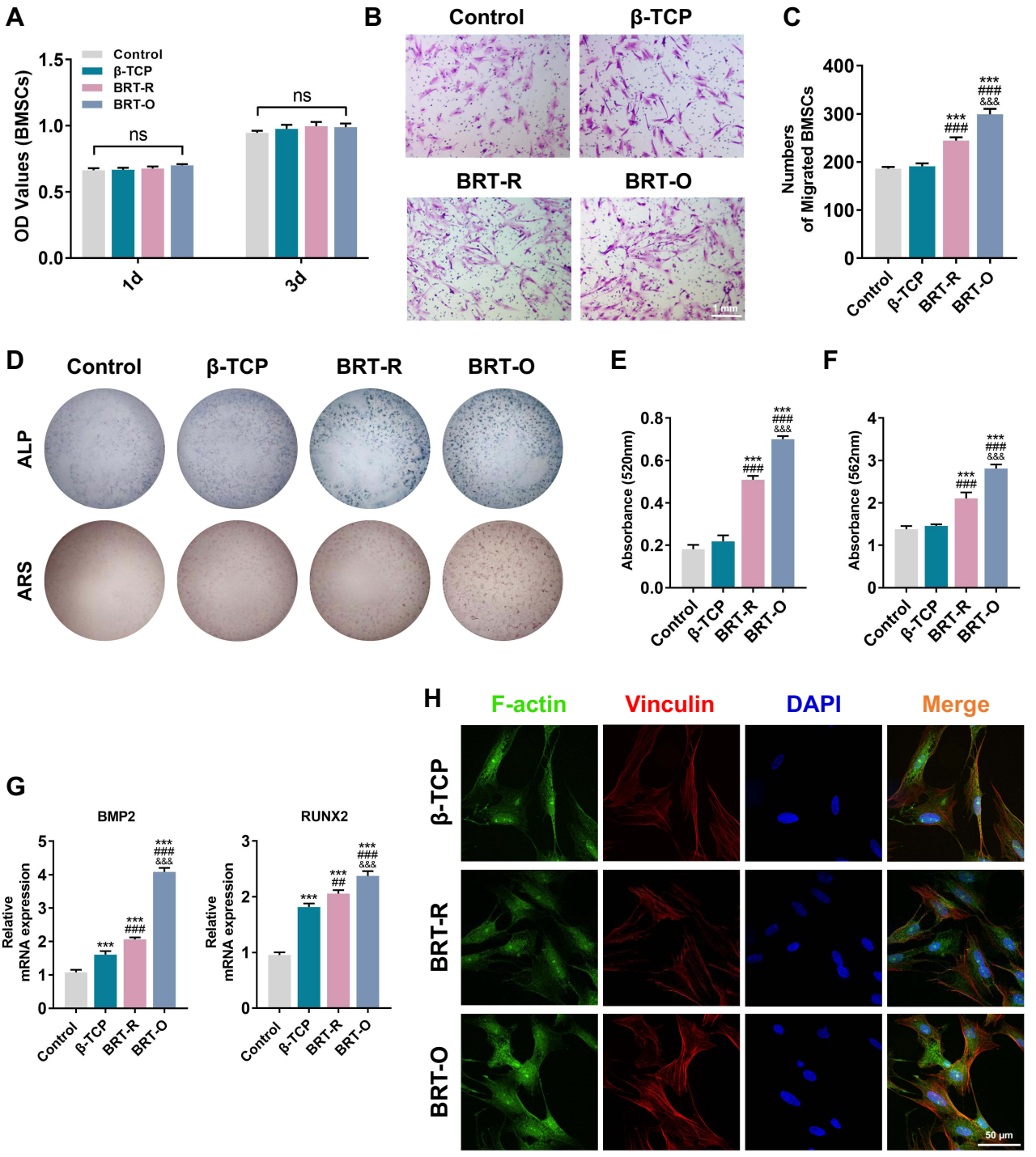

Figure 3 BMSCs proliferation, migration, and differentiation in response to the polarized macrophages by scaffolds. (**A**) Effects of macrophage polarization on BMSCs proliferation using CCK-8 assay. (**B**) BMSCs migration induced by macrophage polarization using Transwell assays. Scale bar, 1 mm. (**C**) Quantification analysis of cells migration. (**D**) ALP staining for alkaline phosphatase activities and ARS images for calcium deposits of the BMSCs. (**E**) Semi-quantitative data of ALP activity assay. (**F**) Quantified analysis of ARS. (**G**) mRNA expression levels of BMP2 and RUNX2 as measured by qRT-PCR. (**H**) IF images for cytoskeletal proteins F-actin (green), vinculin (red), and DAPI (blue). Scale bar, 50 μm. Data are expressed as mean ± SD (n = 3). Ns, no significance; $^{\#\#}P < 0.01$ vs β-TCP scaffold; $^{***}P < 0.001$ vs Control group; $^{\#\#\#}P < 0.001$ vs β-TCP scaffold; $^{\&\&\&}P < 0.001$ vs BRT-R scaffold.

significantly different between the BRT-R and BRT-O groups at weeks 6 and 12. Moreover, the percentage of newly formed bone in the BRT-R group was significantly increased compared to the β-TCP group. In the blank control group, limited bone formation was observed in the central region surrounded by fibrous connective tissues.

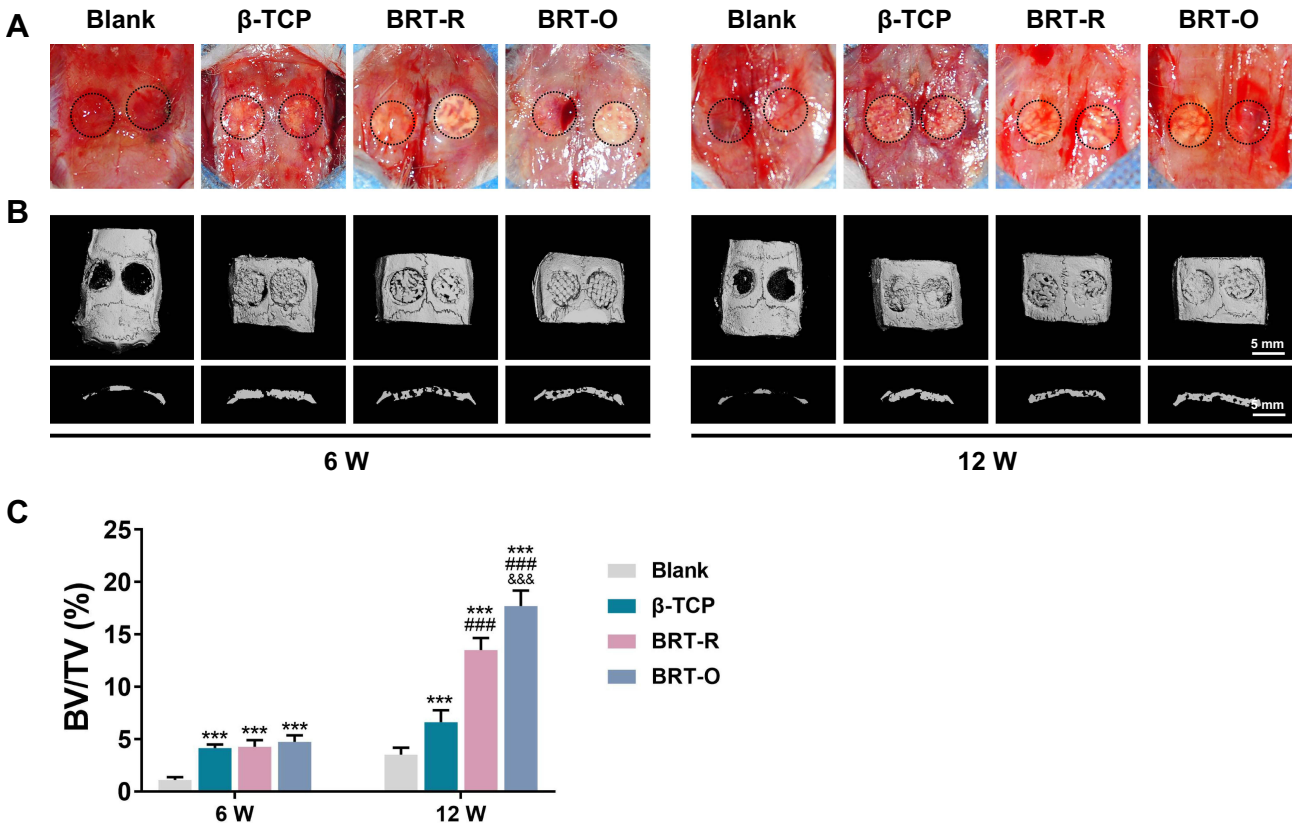

Figure 4 New bone generation as detected by gross observation and μ-CT analysis at weeks 6 and 12 post-implantation. (**A**) Representative gross observation images. (**B**) μ-CT analysis. (**C**) BV/TV as calculated by μ-CT 80 system. Data are expressed as mean ± SD (n = 4). ***$P < 0.001$ vs Control group; $^{\#\#\#}P < 0.001$ vs β-TCP scaffold; $^{\&\&\&}P < 0.001$ vs BRT-R scaffold.

Consistent with the toluidine blue results at week 12, H&E staining exhibited a considerable amount of newly generated bone in the BRT-O group, which completely covered the defect center, in comparison with the other three groups (Figure 5B). In addition, there was a large amount of new bone formed in the defect area of the BRT-R group. In contrast, only limited bone formation was dispersed in the defect region of the β-TCP group (Figure 5C and D). Based on these results, the BRT-O scaffolds markedly enhanced bone regeneration and repaired critical-sized bone defects macroscopically and microscopically.

The Effects of BRT-O on Early-Stage Immunomodulation and Osteogenesis

The markers of osteogenesis and macrophage polarization at one week postoperatively were detected by IHC staining (Figure 6A). On the one hand, early osteogenic marker, RUNX2 positive cells were significantly increased in all three implantation groups, whereas fewer positive cells existed in the blank control group. The BRT-O group had the largest number of positive cells compared to the other two groups. There was hardly any difference between the β-TCP and BRT-R groups regarding RUNX2 expression. Further quantitative analysis of positive cells also confirmed that BRT-O significantly promoted the expression of markers at the early osteogenesis stage in the bone defect areas (Figure 6B).

On the other hand, the expression levels of CD68 (pan-macrophage marker), iNOS (M1 marker), and CD163 (M2 marker) were examined to evaluate an early-stage immune response at the defect sites (Figure 6A). The β-TCP group was without obvious iNOS+-M1 or CD163+-M2 positive macrophage activation, indicating an inert immune response in the β-TCP group. There were markedly higher CD68+iNOS+ M1 macrophage infiltration and fewer CD68+CD163+ M2 macrophage activation around the BRT-R group. More CD68+CD163+ M2 macrophages were gathering around the defect area in the BRT-O group than those in the other three groups. Moreover, cells distribution was roughly speculated from the histological sections. Stem cells and macrophages were at the forefront of tissue-material interface, namely the

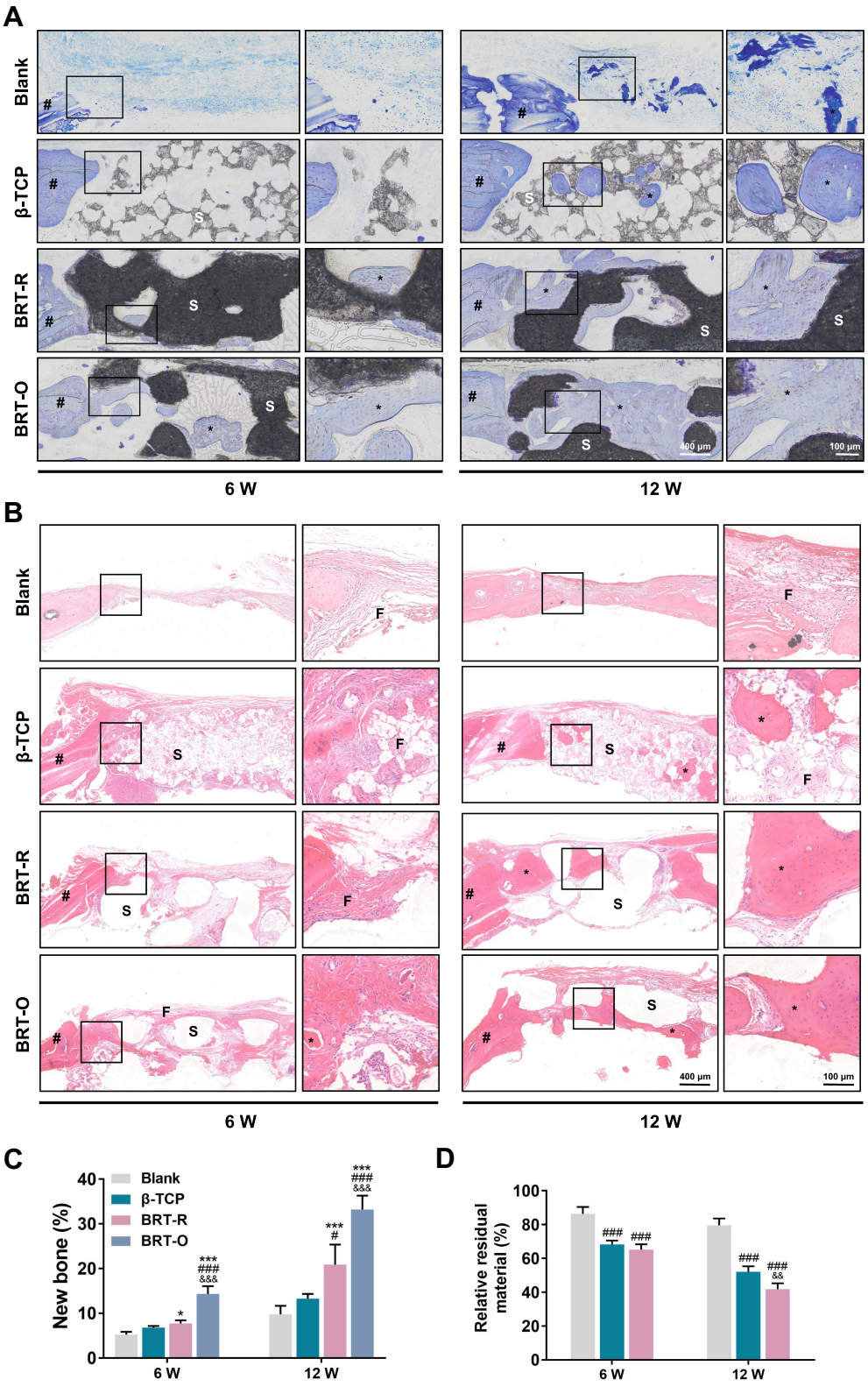

Figure 5 Bone regeneration in the rat cranial critical-sized defect models. (**A**) Representative toluidine blue staining images postoperatively at weeks 6 and 12. (**B**) Representative H&E staining images at weeks 6 and 12 post-implantation. (**C**) Quantified data of new bone percentages in the defects. (**D**) Percentages of relative residual materials according to H&E staining. Data are expressed as mean ± SD (n = 4). The original areas of representative magnification images were outlined with the blank rectangles. Scale bar, 400 μm and 100 μm. $^{*}P < 0.05$ vs Control group; $^{\#}P < 0.05$ vs β-TCP scaffold; $^{\&\&}P < 0.01$ vs BRT-R scaffold; $^{***}P < 0.001$ vs Control group; $^{\#\#\#}P < 0.001$ vs β-TCP scaffold; $^{\&\&\&}P < 0.001$ vs BRT-R scaffold.

Abbreviations: #, old bone; *, new bone; S, scaffolds; F, fibrous connective tissue.

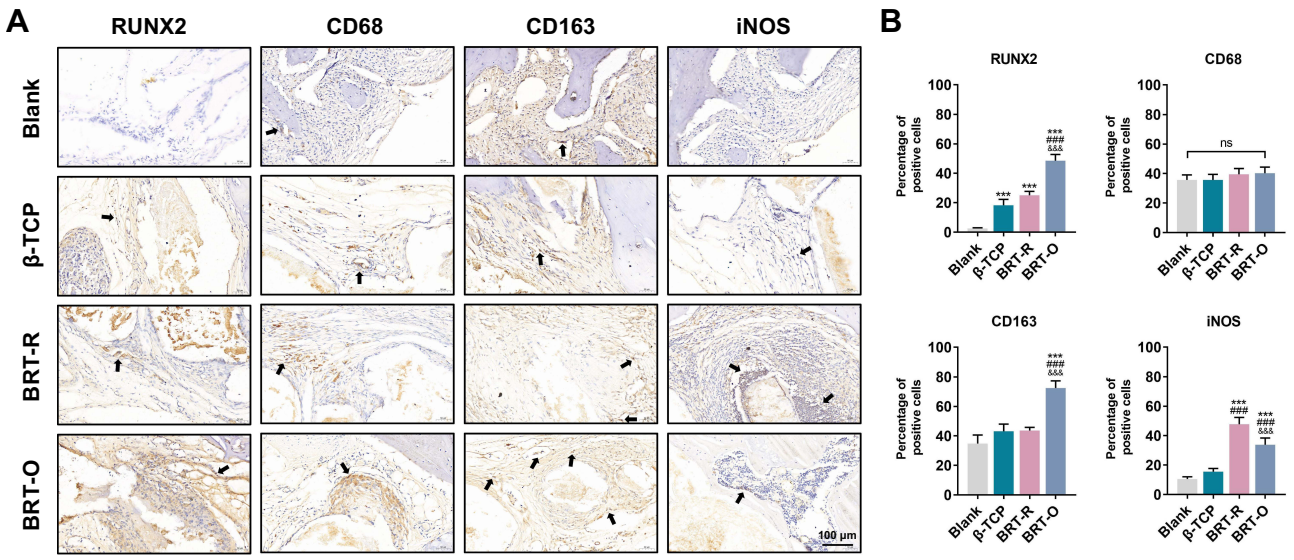

Figure 6 Immunomodulation and osteogenesis in the defect region at one-week post surgery. Positively stained cells are indicated by arrows. (**A**) Representative images of IHC staining for osteogenesis markers RUNX2 expression, macrophage polarization pan marker CD68, M1 marker iNOS, and M2 marker CD163 expression in defect tissues. (**B**) Semi-quantification of RUNX2, CD68, iNOS and CD163 positive cells. Data are expressed as mean ± SD (n = 4). Scale bar, 100 μm. Ns, no significance; $^{***}P < 0.001$ vs Control group; $^{\#\#\#}P < 0.001$ vs β-TCP scaffold; $^{\&\&\&}P < 0.001$ vs BRT-R scaffold.

repairing area. These findings were further confirmed by semi-quantification of IHC staining (Figure 6B), indicating that in the early immune microenvironment of bone defect repair, the BRT-O scaffolds recruited macrophages and orchestrated M1-to-M2 macrophage polarization to facilitate bone regeneration.

Discussion

Recent studies demonstrate that organized topography yields better results regarding tissue regeneration versus disorganized structures,[30,31] yet the concrete mechanism remains obscure. In this study, the fabricated BRT-O scaffolds were structurally ordered at the macro and micro levels using a 3D printing technology for the first time. The novelty of this study lies in that we prepared highly uniform BRT-O scaffolds with excellent physio-chemical properties and biological activities possessing better ability to promote pro-healing M2 macrophage polarization and following bone regeneration, highlighting the promising prospects of aligned bredigite material on osteoimmunomodulation and bone tissue engineering.

The differences in the surface topology of 3D-printed bredigite scaffolds significantly influenced the efficacy of implanted biomaterials. Meanwhile, our results partially demonstrated the relationship between biomaterial surface topography and macrophage polarization and bone regeneration, thereby revealing the potential value of biomaterial surface topography manipulation on the outcomes of bone regeneration. Critical-sized bone defects pose new requirements for the application of biomaterials to achieve the balance of cell viability, function, and mechanical integrity under load-bearing conditions.[4] Unfortunately, the clinical performance of currently available calcium-phosphorus bioceramics is insufficient due to poor mechanical properties.[5] Wu et al developed pure bredigite bioactive ceramic to overcome this shortcoming, demonstrating bending strength and Young's modulus similar to that of natural cortical bone and providing initial stabilization.[9,11] Moreover, Hu et al reposted dose-dependent antibacterial effects of bredigite ceramics.[32] Accompanied by the advancements in 3D printing technology and a better understanding of biomaterials surface topology, we designed structurally ordered bredigite scaffolds with uniform porosity distribution, and we found their enhanced physicochemical properties, higher release of bioactive ions, and reasonable biodegradation compared to the disordered scaffolds.

Macrophages play an important role in the process of biomaterials-induced bone regeneration, where the change of material surface topography modifies their shape and phenotype to some extent.[31] In the present study, macrophages on the surface of BRT-O highly expressed M2 typical markers as detected by flow cytometry, PCR and IF detection, while

the BRT-R group expressed higher M1 marker molecules. Meanwhile, macrophages on the surface of BRT-O stretched longer elongation. Previous studies suggested a close relationship between macrophage shape and activation status, whereas the feedback from macrophage shape may regulate their phenotype.[31,33,34] For instance, elongated macrophages secrete more IL-10 and anti-inflammatory cytokines associated with polarizing to the M2-type. Altogether, ordered and disordered BRT scaffolds can independently induce macrophage polarization toward anti-inflammatory M2 and pro-inflammatory M1 phenotypes.

In addition to the effects on inflammatory and immune response, macrophages are widely recognized to influence the stem cell recruitment and differentiation in biomaterials-related bone healing.[35,36] Considering the differences in macrophage polarization on different scaffold surfaces, we examined how macrophages plasticity shaped the BMSCs osteogenesis. Our data suggested that polarized macrophages induced by the BRT-O scaffolds significantly contributed to the mineralization capacity and osteogenic differentiation of BMSCs in vitro and bone regeneration in vivo, particularly upregulating the transcriptional and translational expression of BMP2 and RUNX2. As an osteoinductor to promote osteogenic differentiation of mesenchymal stem cells, BMP2 is a key protein in the development and homeostasis of skeletal tissues.[37] BMP2 is also produced and regulated by macrophages, especially the M2 type.[38–40] Furthermore, our results showed a noticeable increase in the longitudinal migration capacity of stem cells compared to the BRT-R and β-TCP scaffolds, suggesting a continuous process of bone regeneration. Previous study showed that bredigite ceramics scaffolds facilitated the adherence and spread of osteoblasts on the surface.[9,10] Meanwhile, as reported by Chen et al, bredigite extracts significantly promoted human dental pulp cells (hDPCs) growth, proliferation, and multilineage differentiation, whereas β-TCP extracts lacked these properties.[13]

On the one hand, the osteoimmunomodulation of biomaterials originates from the release of bioactive ions. Ca and Mg are two essential elements in the natural bone tissues affecting bone regeneration directly.[1] The intracellular and extracellular calcium levels can also regulate the polarized phenotype of macrophages.[41] Magnesium is thought to fight inflammation, regulate macrophage-mediated inflammatory responses, and promote osseointegration.[42] Si is another important bioactive ion in the human body, whereas the SiO_4-group in silicate-based biomaterials is essential for inducing early mineralization during new bone formation,[43–45] and markedly facilitating osteoblast growth and differentiation.[46,47] Accordingly, Si ions released from the 3D-printed silicate scaffolds can polarize macrophages to the M2 phenotype.[48] Wu et al observed that ionic products from bredigite dissolution significantly promoted the proliferation and cementogenic differentiation of periodontal ligament stem cells (PDLSCs).[14] Bioactive ions can also modulate immunity and macrophage polarization phenotype.[49] Our study reported similar findings as stable and mild degradation and continuous release of ionic products was observed over a long period of time in Tris solution.

On the other hand, physical cues particular in topology contributes to the osteoimmunomodulatory properties of the biomaterial.[49,50] First, scaffold materials with appropriate porosity and porous structure facilitate the growth and differentiation of stem cells, adhesion and activation of macrophages, which are crucial for the fate of macrophage activation.[51,52] Mesopores (>100 μm) and macropores (>300 μm) were believed to enhance cell adhesion, proliferation, and ingrowth of newly formed tissues.[53] The BRT-O materials synthesized in this study had a large-sized porosity (400~500 μm), providing better affinity for BMSCs and macrophages. Natural bone is a highly ordered tissue, and structurally ordered 3D printed materials achieved greater degree of biomimicry. Structurally ordered nanofiber scaffolds significantly enhanced the proliferation and differentiation of stem cells compared to disordered fibers and promoted the differentiation of macrophages to the M2 type.[31]

Therefore, it is reasonable to assume that 3D-printed BRT-O scaffolds can significantly modulate the immune microenvironment of macrophages that may satisfy the demand for physicochemical properties and biological activity for biomaterials, especially for the repair of critical-sized bone defects. In this study, topographical cues were proposed to influence the outcome of macrophage polarization and bone regeneration following the implantation of 3D-printed scaffolds, while excluding differences in chemical composition. These findings suggested that manipulating the physical structure may provide important directions for future biomaterial design.[36] However, further experimental evidence and clinical studies are still needed to explore the deep mechanism of materials topology and to update the clinical usability of BRT-O materials in the future. Furthermore, considering the multiple intermediate states of macrophages transition, sequencing technology can be used to determine more accurate polarization in further studies.

Conclusion

In this study, we successfully fabricated ordered bredigite (BRT-O) scaffolds with a well-organized structure and regular morphology. The 3D-printed BRT-O scaffolds exhibited excellent mechanical properties and controlled release of bioactive ionic products. More importantly, the BRT-O scaffolds significantly promoted macrophage polarization to the M2 phenotype, which provided favorable conditions for BMSCs migration and osteogenic differentiation. In vivo, BRT-O scaffolds constructed the osteoinductive microenvironment benefiting bone regeneration in the rat cranial bone defect models by adjusting the immune response. Therefore, the 3D-printed BRT-O scaffolds can be a promising option for bone tissue engineering through macrophages polarization and osteoimmunomodulation.

Acknowledgments

This work was supported by the National Key R&D Program of China (2020YFC2008900), the National Natural Science Foundation of China (81900968) and the Shanghai Sailing Program (19YF1426100).

Disclosure

The authors report no conflicts of interest in this work.

References

1. Zhang W, Feng C, Yang G, et al. 3D-printed scaffolds with synergistic effect of hollow-pipe structure and bioactive ions for vascularized bone regeneration. *Biomaterials*. 2017;135:85–95. doi:10.1016/j.biomaterials.2017.05.005
2. Feng Y, Zhu S, Mei D, et al. Application of 3D printing technology in bone tissue engineering: a review. *Curr Drug Deliv*. 2021;18(7):847–861. doi:10.2174/1567201817999201113100322
3. Cheng L, Suresh KS, He H, et al. 3D printing of micro- and nanoscale bone substitutes: a review on technical and translational perspectives. *Int J Nanomedicine*. 2021;16:4289–4319. doi:10.2147/ijn.S311001
4. Zhang L, Yang G, Johnson BN, Jia X. Three-dimensional (3D) printed scaffold and material selection for bone repair. *Acta Biomater*. 2019;84:16–33. doi:10.1016/j.actbio.2018.11.039
5. Shao H, Sun M, Zhang F, et al. Custom repair of mandibular bone defects with 3D printed bioceramic scaffolds. *J Dent Res*. 2018;97(1):68–76. doi:10.1177/0022034517734846
6. Bose S, Roy M, Bandyopadhyay A. Recent advances in bone tissue engineering scaffolds. *Trends Biotechnol*. 2012;30(10):546–554. doi:10.1016/j.tibtech.2012.07.005
7. Zafar MS, Khurshid Z, Almas K. Oral tissue engineering progress and challenges. *Tissue Eng Regen Med*. 2015;12(6):387–397. doi:10.1007/s13770-015-0030-6
8. Eilbagi M, Emadi R, Raeissi K, Kharaziha M, Valiani A. Mechanical and cytotoxicity evaluation of nanostructured hydroxyapatite-bredigite scaffolds for bone regeneration. *Mater Sci Eng C Mater Biol Appl*. 2016;68:603–612. doi:10.1016/j.msec.2016.06.030
9. Wu C, Chang J, Wang J, Ni S, Zhai W. Preparation and characteristics of a calcium magnesium silicate (bredigite) bioactive ceramic. *Biomaterials*. 2005;26(16):2925–2931. doi:10.1016/j.biomaterials.2004.09.019
10. Wu C, Chang J, Zhai W, Ni S. A novel bioactive porous bredigite (Ca7MgSi4O16) scaffold with biomimetic apatite layer for bone tissue engineering. *J Mater Sci Mater Med*. 2007;18(5):857–864. doi:10.1007/s10856-006-0083-0
11. Wu C, Chang J. Synthesis and in vitro bioactivity of bredigite powders. *J Biomater Appl*. 2007;21(3):251–263. doi:10.1177/0885328206062360
12. Yi D, Wu C, Ma B, Ji H, Zheng X, Chang J. Bioactive bredigite coating with improved bonding strength, rapid apatite mineralization and excellent cytocompatibility. *J Biomater Appl*. 2014;28(9):1343–1353. doi:10.1177/0885328213508165
13. Chen L, Liu L, Wu C, Yang R, Chang J, Wei X. The extracts of bredigite bioceramics enhanced the pluripotency of human dental pulp cells. *J Biomed Mater Res A*. 2017;105(12):3465–3474. doi:10.1002/jbm.a.36191
14. Zhou Y, Wu C, Zhang X, Han P, Xiao Y. The ionic products from bredigite bioceramics induced cementogenic differentiation of periodontal ligament cells via activation of the Wnt/β-catenin signalling pathway. *J Mater Chem B*. 2013;1(27):3380–3389. doi:10.1039/c3tb20445f
15. Zheng Z, Chen Y, Wu D, et al. Development of an accurate and proactive immunomodulatory strategy to improve bone substitute material-mediated osteogenesis and angiogenesis. *Theranostics*. 2018;8(19):5482–5500. doi:10.7150/thno.28315
16. Luttikhuizen D, Harmsen M, Van Luyn M. Cellular and molecular dynamics in the foreign body reaction. *Tissue Eng*. 2006;12(7):1955–1970. doi:10.1089/ten.2006.12.1955
17. Londono R, Badylak S. Biologic scaffolds for regenerative medicine: mechanisms of in vivo remodeling. *Ann Biomed Eng*. 2015;43(3):577–592. doi:10.1007/s10439-014-1103-8
18. Xie Y, Hu C, Feng Y, et al. Osteoimmunomodulatory effects of biomaterial modification strategies on macrophage polarization and bone regeneration. *Regen Biomater*. 2020;7(3):233–245. doi:10.1093/rb/rbaa006
19. Anderson J, Rodriguez A, Chang D. Foreign body reaction to biomaterials. *Semin Immunol*. 2008;20(2):86–100. doi:10.1016/j.smim.2007.11.004
20. Mantovani A, Biswas SK, Galdiero MR, Sica A, Locati M. Macrophage plasticity and polarization in tissue repair and remodelling. *J Pathol*. 2013;229(2):176–185. doi:10.1002/path.4133
21. Jin SS, He DQ, Luo D, et al. A biomimetic hierarchical nanointerface orchestrates macrophage polarization and mesenchymal stem cell recruitment to promote endogenous bone regeneration. *ACS Nano*. 2019;13(6):6581–6595. doi:10.1021/acsnano.9b00489
22. Locati M, Curtale G, Mantovani A. Diversity, mechanisms, and significance of macrophage plasticity. *Annu Rev Pathol*. 2020;15:123–147. doi:10.1146/annurev-pathmechdis-012418-012718

23. Rostam H, Singh S, Vrana N, Alexander M, Ghaemmaghami A. Impact of surface chemistry and topography on the function of antigen presenting cells. *Biomater Sci*. 2015;3(3):424–441. doi:10.1039/c4bm00375f
24. Hasan A, Byambaa B, Morshed M, et al. Advances in osteobiologic materials for bone substitutes. *J Tissue Eng Regen Med*. 2018;12 (6):1448–1468. doi:10.1002/term.2677
25. Chen Z, Bachhuka A, Wei F, et al. Nanotopography-based strategy for the precise manipulation of osteoimmunomodulation in bone regeneration. *Nanoscale*. 2017;9(46):18129–18152. doi:10.1039/c7nr05913b
26. Yang Y, Lin Y, Zhang Z, Xu R, Yu X, Deng F. Micro/nano-net guides M2-pattern macrophage cytoskeleton distribution via Src-ROCK signalling for enhanced angiogenesis. *Biomater Sci*. 2021;9(9):3334–3347. doi:10.1039/d1bm00116g
27. McMurray RJ, Gadegaard N, Tsimbouri PM, et al. Nanoscale surfaces for the long-term maintenance of mesenchymal stem cell phenotype and multipotency. *Nat Mater*. 2011;10(8):637–644. doi:10.1038/nmat3058
28. Prendergast M, Burdick J. Recent advances in enabling technologies in 3D printing for precision medicine. *Adv Mater*. 2020;32(13):e1902516. doi:10.1002/adma.201902516
29. Seo SJ, Mahapatra C, Singh RK, Knowles JC, Kim HW. Strategies for osteochondral repair: focus on scaffolds. *J Tissue Eng*. 2014;5:2041731414541850. doi:10.1177/2041731414541850
30. Daghrery A, Ferreira JA, Xu J, et al. Tissue-specific melt electrowritten polymeric scaffolds for coordinated regeneration of soft and hard periodontal tissues. *Bioact Mater*. 2023;19:268–281. doi:10.1016/j.bioactmat.2022.04.013
31. Jia Y, Yang W, Zhang K, et al. Nanofiber arrangement regulates peripheral nerve regeneration through differential modulation of macrophage phenotypes. *Acta Biomater*. 2019;83:291–301. doi:10.1016/j.actbio.2018.10.040
32. Hu S, Ning C, Zhou Y, Chen L, Lin K, Chang J. Antibacterial activity of silicate bioceramics. *J Wuhan Univ Technol Mater Sci Ed*. 2011;26 (2):226–230. doi:10.1007/s11595-011-0202-8
33. McWhorter FY, Wang T, Nguyen P, Chung T, Liu WF. Modulation of macrophage phenotype by cell shape. *Proc Natl Acad Sci USA*. 2013;110 (43):17253–17258. doi:10.1073/pnas.1308887110
34. Li K, Lv L, Shao D, Xie Y, Cao Y, Zheng X. Engineering nanopatterned structures to orchestrate macrophage phenotype by cell shape. *J Funct Biomater*. 2022;13(1):31. doi:10.3390/jfb13010031
35. Pajarinen J, Lin T, Gibon E, et al. Mesenchymal stem cell-macrophage crosstalk and bone healing. *Biomaterials*. 2019;196:80–89. doi:10.1016/j.biomaterials.2017.12.025
36. Li J, Jiang X, Li H, Gelinsky M, Gu Z. Tailoring materials for modulation of macrophage fate. *Adv Mater*. 2021;33(12):e2004172. doi:10.1002/adma.202004172
37. Larochette N, El-Hafci H, Potier E, et al. Osteogenic-differentiated mesenchymal stem cell-secreted extracellular matrix as a bone morphogenetic protein-2 delivery system for ectopic bone formation. *Acta Biomater*. 2020;116:186–200. doi:10.1016/j.actbio.2020.09.003
38. Wu M, Chen G, Li YP. TGF-β and BMP signaling in osteoblast, skeletal development, and bone formation, homeostasis and disease. *Bone Res*. 2016;4:16009. doi:10.1038/boneres.2016.9
39. Chen Z, Wu C, Gu W, Klein T, Crawford R, Xiao Y. Osteogenic differentiation of bone marrow MSCs by β-tricalcium phosphate stimulating macrophages via BMP2 signalling pathway. *Biomaterials*. 2014;35(5):1507–1518. doi:10.1016/j.biomaterials.2013.11.014
40. Kim YH, Oreffo ROC, Dawson JI. From hurdle to springboard: the macrophage as target in biomaterial-based bone regeneration strategies. *Bone*. 2022;159:116389. doi:10.1016/j.bone.2022.116389
41. Kang H, Zhang K, Wong DSH, Han F, Li B, Bian L. Near-infrared light-controlled regulation of intracellular calcium to modulate macrophage polarization. *Biomaterials*. 2018;178:681–696. doi:10.1016/j.biomaterials.2018.03.007
42. Qiao X, Yang J, Shang Y, et al. Magnesium-doped nanostructured titanium surface modulates macrophage-mediated inflammatory response for ameliorative osseointegration. *Int J Nanomedicine*. 2020;15:7185–7198. doi:10.2147/ijn.S239550
43. Schwarz K, Milne D. Growth-promoting effects of silicon in rats. *Nature*. 1972;239(5371):333–334. doi:10.1038/239333a0
44. Carlisle E. Silicon: a possible factor in bone calcification. *Science*. 1970;167(3916):279–280. doi:10.1126/science.167.3916.279
45. Liu X, Ding C, Chu PK. Mechanism of apatite formation on wollastonite coatings in simulated body fluids. *Biomaterials*. 2004;25(10):1755–1761. doi:10.1016/j.biomaterials.2003.08.024
46. Pei P, Qi X, Du X, Zhu M, Zhao S, Zhu Y. Three-dimensional printing of tricalcium silicate/mesoporous bioactive glass cement scaffolds for bone regeneration. *J Mater Chem B*. 2016;4(46):7452–7463. doi:10.1039/c6tb02055k
47. Zhai W, Lu H, Wu C, et al. Stimulatory effects of the ionic products from Ca-Mg-Si bioceramics on both osteogenesis and angiogenesis in vitro. *Acta Biomater*. 2013;9(8):8004–8014. doi:10.1016/j.actbio.2013.04.024
48. Li T, Peng M, Yang Z, et al. 3D-printed IFN-γ-loading calcium silicate-β-tricalcium phosphate scaffold sequentially activates M1 and M2 polarization of macrophages to promote vascularization of tissue engineering bone. *Acta Biomater*. 2018;71:96–107. doi:10.1016/j.actbio.2018.03.012
49. Bai X, Liu W, Xu L, et al. Sequential macrophage transition facilitates endogenous bone regeneration induced by Zn-doped porous microcrystalline bioactive glass. *J Mater Chem B*. 2021;9(12):2885–2898. doi:10.1039/d0tb02884c
50. Chen Z, Bachhuka A, Han S, et al. Tuning chemistry and topography of nanoengineered surfaces to manipulate immune response for bone regeneration applications. *ACS Nano*. 2017;11(5):4494–4506. doi:10.1021/acsnano.6b07808
51. Zhang R, Elkhooly TA, Huang Q, et al. Effects of the hierarchical macro/mesoporous structure on the osteoblast-like cell response. *J Biomed Mater Res A*. 2018;106(7):1896–1902. doi:10.1002/jbm.a.36387
52. Murphy CM, Haugh MG, O'Brien FJ. The effect of mean pore size on cell attachment, proliferation and migration in collagen-glycosaminoglycan scaffolds for bone tissue engineering. *Biomaterials*. 2010;31(3):461–466. doi:10.1016/j.biomaterials.2009.09.063
53. Chen L, Deng C, Li J, et al. 3D printing of a lithium-calcium-silicate crystal bioscaffold with dual bioactivities for osteochondral interface reconstruction. *Biomaterials*. 2019;196:138–150. doi:10.1016/j.biomaterials.2018.04.005